An Islanding Detection Method Using Synchronized Small-AC-Signal Injection for Grid-Forming Inverters in Microgrids

Haoyang Zheng, *Graduate Student Member, IEEE*, Zeng Liu, *Senior Member, IEEE*, Ronghui An, *Member, IEEE*, Jinjun Liu, *Fellow, IEEE*, Tong Wu, *Student Member, IEEE*, and Zhenhuang Lin

***Abstract*—Islanding detection is of great importance for the microgrid in order to change the control objectives and to avoid unsynchronized reclosure. Active islanding detection methods based on impedance measurement have very small nondetection zone in the single-inverter system, but require the coordination of the perturbation current injected by each inverter in the microgrid consisting of multiple inverters. The conventional solution by injecting a harmonic current synchronized with the fundamental output voltage is affected by different winding connections in grid-side transformers of inverters and degrades the voltage quality in stand-alone mode. This article proposes an islanding detection method based on impedance measurement for the microgrid comprised of grid-forming inverters with seamless transfer capabilities. The proposed method achieves synchronized injection of small-ac-signal (SACS) current using the SACS current droop control and the virtual impedance. The synchronized SACS current injection in the proposed method is independent of fundamental components and is not influenced by different winding connections in grid-side transformers of inverters. Moreover, the SACS current limiting control is introduced to mitigate the impact of injected SACS current on the grid current quality. In addition, the control scheme is peer-to-peer and enables plug-and-play functionality. The effectiveness and advantages of the proposed method are validated through simulation and experimental results.**

***Index Terms*—Impedance measurement, islanding, microgrids, voltage source inverters.**

I. Introduction

UNDER the background of rising energy demand and environmental concerns, the microgrid (MG) concept was proposed to integrate distributed generators (DGs) in a more reliable and more efficient way by viewing generation, load, storage device, and the transfer switch with the utility grid as a subsystem, aiming to operate both in grid-connected (GC) mode to inject power to the utility grid, and in stand-alone (SA) mode to provide uninterrupted power to critical load [1], [2], [3].

The MG should be able to seamlessly transfer between GC and SA modes to ensure the uninterrupted power supply to critical loads. Grid-following (GFL) inverters are conventionally used in GC mode, which are controlled as current sources and generally synchronize with the grid through a phase-locked loop (PLL). However, GFL inverters tend to be unstable in SA mode when the load-matching condition is not satisfied [4]. Therefore, reconfiguration of control scheme is necessary to provide voltage support when the MG transfers from GC mode to SA mode. Many mode transition strategies based on GFL inverters need the islanding detection information [5], [6], so the voltage quality may be deteriorated before the confirmation of islanding detection. The seamless transfer methods proposed in [7] and [8] do not rely on islanding detection, but they focus on single-inverter systems. Grid-forming (GFM) inverters, which are controlled as flexible voltage sources and synchronize with the grid through frequency droop control, are emerging as a promising solution for integration of renewable energies, since they show enhanced stability in weak grids, and can naturally operate in SA mode [4], [9]. Some seamless transfer methods based on GFM inverters have been proposed [10], [11], [12], [13]. Among them, the method in [10] achieves seamless transfer in a peer-to-peer manner in the MG by limiters in the output current loop without the need of fast islanding detection. The method in [13] further simplified the control scheme by removing the PLL in GC mode in [10].

For MGs comprised of GFM inverters with seamless transfer capabilities by using limiters, islanding detection is still important for the following major reasons [4], [13]:

1) the MG side static switch should be turned OFF after islanding to avoid unsynchronized reclosure;
2) the control objectives are different in SA mode and GC mode, and the seamless transfer strategy cannot provide accurate information on operation mode;
3) it is better to remove the outputs of the limiters associated with seamless transfer after the islanding to improve the

Manuscript received 20 August 2022; revised 27 November 2022; accepted 6 January 2023. Date of publication 17 January 2023; date of current version 10 March 2023. This work was supported in part by the National Key Research and Development Program of China under Grant 2018YFB1503101 and in part by the Natural Science Basic Research Program of Shaanxi under Grant 2020JM-060. Recommended for publication by Associate Editor S. Golestan. This paper was presented in part at the 2020 IEEE 9th International Power Electronics and Motion Control Conference (IPEMC 2020 - ECCE Asia), Nanjing, China, Nov. 29–Dec. 2, 2020. *(Corresponding author: Zeng Liu.)*

Haoyang Zheng, Zeng Liu, Ronghui An, Jinjun Liu, and Tong Wu are with the State Key Laboratory of Electrical Insulation and Power Equipment, School of Electrical Engineering, Xi'an Jiaotong University, Xi'an 710049, China (e-mail: apusong30@stu.xjtu.edu.cn; zengliu@mail.xjtu.edu.cn; an_ronghui@163.com; jjliu@mail.xjtu.edu.cn; tonywu@stu.xjtu.edu.cn).

Zhenhuang Lin is with the Kehua Data Company, Ltd., Xiamen 361006, China (e-mail: linzhenhuang@kehua.com).

Color versions of one or more figures in this article are available at https://doi.org/10.1109/TPEL.2023.3237569.

Digital Object Identifier 10.1109/TPEL.2023.3237569

voltage quality. Therefore, it is better to combine seamless transfer strategy with islanding detection.

Islanding detection methods can be classified into three categories: communication-based methods, passive methods, and active methods. Communication-based methods are efficient but costly, and face the risk of communication failure [11]. Passive methods monitor some local variables such as frequency, voltage amplitude, and harmonic content to detect islanding [14], [15], [16], [17], but they generally have large nondetection zone (NDZ). Active methods inject some disturbance into the system and monitor the related response. Among the active methods, the methods based on local impedance measurement do not cause degradation of the fundamental voltage after the islanding as the active frequency drift methods [18], [19] or the power variation methods [20], [21], and thus do not conflict with seamless transfer. Besides, they have reduced or zero NDZ [22]. Therefore, the methods based on local impedance measurement are promising for MGs. The disturbance injected into the grid for impedance measurement, such as harmonic/interharmonic voltage or current, is referred to as small-ac-signal (SACS) in this article.

The coordination of SACS injection in MGs consisting of multiple inverters is an important issue. The interaction resulted from uncoordinated injection may lead to the failure of islanding detection [23], [24], [25]. To achieve coordination, mainly two strategies exist. The first strategy is to only allow one inverter to inject SACS, while the other inverters behave as large impedance at the SACS frequency [26], [27], [28]. These methods are not peer-to-peer due to unequal statuses of the inverters. Besides, they are all based on GFL inverters, so the voltage quality may degrade before the confirmation of islanding detection, violating the requirement of seamless transfer. The methods [26], [27] are based on master-slave SACS voltage injection scheme, where the failure of master inverter should be handled. In the method [28], the inverters inject SACS current in turns. However, the injection sequence should be modified in case of any newly added inverter.

The second strategy to achieve coordination is to let multiple inverters inject synchronized SACS currents of almost the same amplitude and phase angle. This strategy is more appealing, since each inverter can detect the islanding based on local impedance measurement in a peer-to-peer manner, thus higher reliability is achieved. To achieve synchronized SACS current injection without additional communication, the most popular method is to synchronize the SACS current injected by the GFL inverters with a common reference, which is usually the fundamental output voltage [23], [24], [29], [30], [31], whose phase angle differs little for each inverter. However, as mentioned earlier, the GFL inverters are not compatible with seamless transfer. Besides, the synchronization is affected by the fundamental voltage, and therefore, by fundamental power sharing. Moreover, when transformers are implemented, where the winding connections may change the relative location between the fundamental voltage and SACS current, predefined time delays should be set accordingly, otherwise the synchronization may not be achieved [23]. In addition, current injection results in large voltage distortion in SA mode. The method proposed in [31] changes the current injection to voltage injection when the MG transfers from GC mode to SA mode to mitigate the voltage distortion. However, in SA mode the phase of SACS voltage instead of the phase of SACS current is synchronized with the fundamental output voltage, so the synchronization in SA mode greatly depends on power sharing ratio.

This article proposes an active islanding detection method based on impedance measurement with synchronized SACS injection for the MG comprised of GFM inverters with seamless transfer capabilities. The SACS synchronization is realized by the SACS droop control and SACS virtual impedance. The existing active islanding detection methods based on coordinated SACS injection and the proposed method are compared in Table I. The synchronization of SACS injection using the proposed method is independent of fundamental components in the steady state, and is not affected by different winding connections in the grid-side transformers of inverters. Moreover, the impact of the SACS injection on the grid current quality is mitigated by introducing the SACS current limiting control. In addition, the control scheme is peer-to-peer and enables plug-and-play functionality, which means that a new inverter can be plugged into the MG without reconfiguration of control scheme. Finally, comprehensive design methodology of key parameters is also provided based on small-signal modeling and restrictions of power quality imposed by the grid codes.

The remainder of this article is organized as follows. In Section II, the studied MG consisting of GFM inverters with seamless transfer capabilities is introduced. The proposed islanding detection method is introduced in detail in Section III. Comprehensive parameter design is given in Section IV. Simulation and experimental results are given in Section V to verify the effectiveness of the proposed method. Finally, Section VI concludes this article.

II. Studied MG Consisting of GFM Inverters With Seamless Transfer Capabilities

A. System Configuration

The schematic diagram of the studied three-phase MG system is shown in Fig. 1. Each inverter is GFM, composed of a constant dc voltage source, a three-phase three-leg half-bridge converter, and an LC filter. The inverters may be equipped with grid-side transformers with turns ratio 1:N, and are connected to the point of common coupling (PCC) through inductive line impedance Z_l. Z_l is considered to include the leakage inductance, so that the transformers are considered as ideal. If there is no transformer, N is considered as 1. A load represented by a Y-connected load impedance Z_{load} is connected at the PCC. The number of the inverter is included in the subscript of the variables. The MG is connected to the utility grid through static transfer switch S_i, which is controlled by MG, and breaker S_u, which is governed by protection device of the utility grid. The grid impedance is Z_g. When a grid fault occurs, S_u turns OFF immediately, and the MG works in SA mode. Once the islanding is confirmed, S_i turns OFF. When the utility grid is restored, S_u turns ON, and the MG will reconnect to the grid when the voltages at both sides of S_i

TABLE I
COMPARISON AMONG EXISTING METHODS BASED ON COORDINATED SACS INJECTION AND PROPOSED METHOD

Islanding detection approaches	Impact of winding connection of transformers on islanding detection	Impact of fundamental components on islanding detection	Voltage distortion in SA mode	Current distortion in GC mode	Peer-to-peer capability	Compatibility with seamless transfer
Master-slave injection [26], [27]	None	None	Small	Large	No	No
Injection in turns [28]	None	None	Large	Small	No	No
Synchronized current injection [23], [24], [29], [30]	Large	Medium	Large	Small	Yes	No
Synchronized current and voltage injection [31]	Large	Large	Small	Small	Yes	No
Proposed method	None	None	Small	Small	Yes	Yes

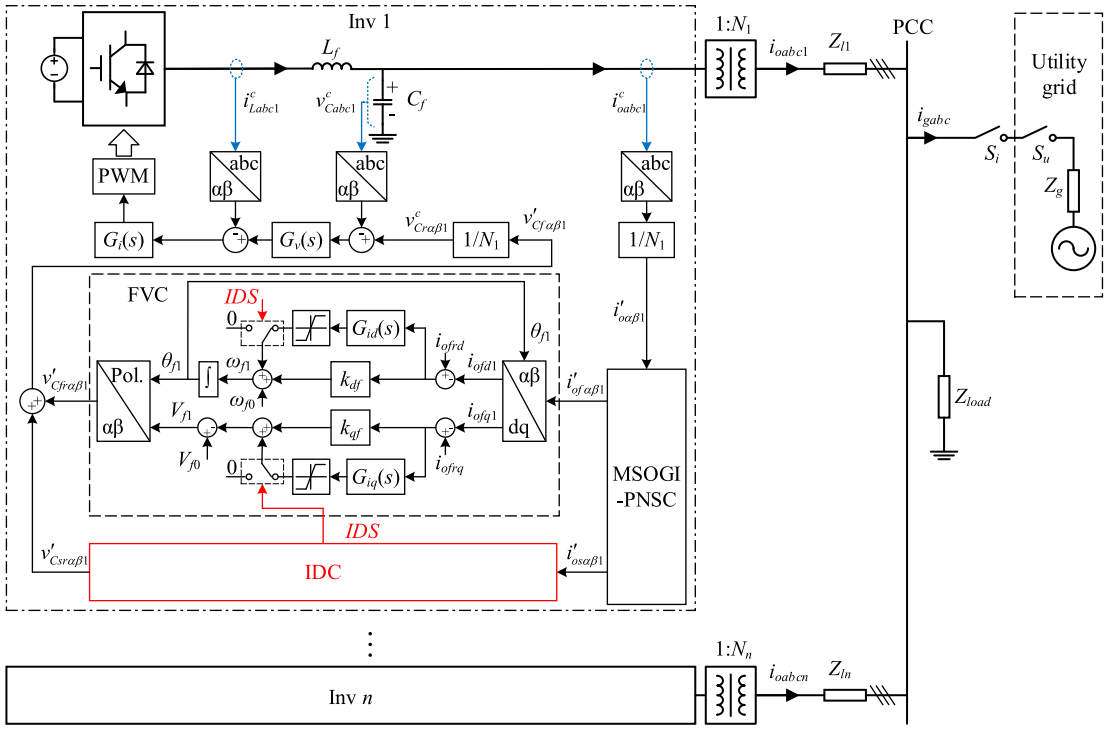

Fig. 1. Configuration of the studied MG consisting of *n* GFM inverters.

are close enough, which can be achieved in an active or passive way [13], [32].

B. Overall Control Block Diagram

Local controllers with the same structure are implemented in the inverters in the studied MG, explicitly shown in Inv 1 below the main circuit in Fig. 1. Each inverter senses its inductor current i^c_{Labc}, capacitor voltage v^c_{Cabc}, and output current i^c_{oabc} to generate the modulation signal. The superscript c denotes the inverter-side variables. The local controller is composed of Clark and inverse Clark transformations, multiple second-order generalized integrators combined with positive-/negative-sequence calculation blocks (MSOGI-PNSC) [33], [34], the fundamental voltage controller (FVC), the proposed islanding detection controller (IDC), and the voltage-current dual loop.

The sampled variables in abc frame are transformed into $\alpha\beta$ frame by the Clark transformation, which is power-invariant. The output $\alpha\beta$-frame current divided by N is noted as $i'_{o\alpha\beta}$, referred to as corrected output current, which has the same amplitude as the PCC-side current, but shows a phase shift determined by the winding connection of the transformer. By this correction, the amplitudes of the reference output voltage components generated by the FVC and the IDC and the amplitudes of the dq variables in the FVC and the IDC are also converted to the PCC side, so the parameters of FVC and IDC in each inverter can be designed regardless of turns ratio.

From $i'_{o\alpha\beta}$, the MSOGI-PNSC extracts fundamental positive sequence component $i'_{of\alpha\beta}$ and SACS positive sequence component $i'_{os\alpha\beta}$, which are sent to the FVC and the IDC, respectively. The block diagram of MSOGI-PNSC is shown in Fig. 2, which contains two parallel-connected dual second-order generalized integrator-quadrature signal generators (DSOGI-QSGs) tuned at the fundamental frequency and the SACS frequency. The resonant frequencies of the two DSOGI-QSGs are updated by ω_f and ω_s from the FVC and the IDC, respectively. The gains of DSOGI-QSGs are k_{SOGIf} and k_{SOGIs}, respectively.

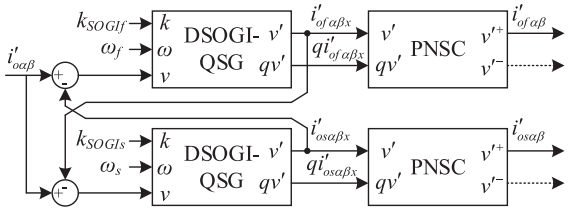

Fig. 2. Block diagram of MSOGI-PNSC for signal extraction.

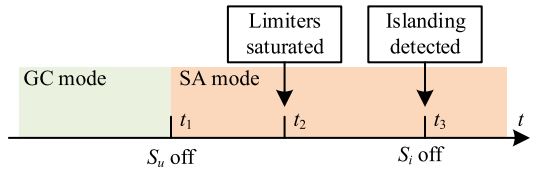

Fig. 3. Sequence diagram of the transition from GC mode to SA mode.

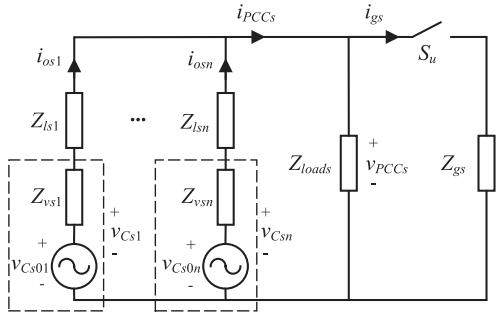

Fig. 4. Equivalent circuit at SACS frequency of the MG with n inverters.

The FVC controls the fundamental components and achieves seamless transfer. The IDC achieves islanding detection, and generates the islanding detection signal *IDS* for the FVC. The corrected reference output voltage $v'_{Cr\alpha\beta}$ is the sum of the corrected fundamental voltage reference $v'_{Cfr\alpha\beta}$ and the corrected SACS voltage reference $v'_{Csr\alpha\beta}$, generated by the FVC and the IDC, respectively. The SACS component is injected for the islanding detection. $v'_{Cr\alpha\beta}$ is divided by N to obtain the inverter-side reference output voltage $v^c_{Cr\alpha\beta}$. For the voltage-current dual loop, the current controller $G_i(s)$ is a proportional controller, and the voltage controller $G_v(s)$ contains two proportional resonant controllers in parallel tuned at the fundamental frequency ω_f and the SACS frequency ω_s to track $v^c_{Cr\alpha\beta}$ without steady-state error, similarly as in [34]. The frequency synchronization of the fundamental component is achieved by fundamental droop control in the FVC, and the frequency synchronization of the SACS component is achieved by the SACS droop control in the proposed IDC.

C. Seamless Transfer

The peer-to-peer seamless transfer method in [13] is adopted in this article, which allows seamless transition from GC to SA mode without reconfiguration of control structure or the information of islanding detection. Some modifications of the original method in [13] are made in this article:

1) inductive line impedance is considered;
2) harmonic compensation is not considered for simplicity;
3) MSOGI-PNSC is used to extract fundamental positive sequence component of the output current;
4) resonant controllers instead of repetitive controller are used in the voltage loop.

In the FVC shown in Fig. 1, $G_{id}(s)$ and $G_{iq}(s)$ are PI controllers with limited outputs in parallel with proportional droop coefficients k_{df} and k_{qf}. This droop control with limiters is referred to as modified droop control. The extracted $i'_{of\alpha\beta}$ from the MSOGI-PNSC is transformed into the dq frame rotating with the fundamental voltage reference angle θ_f, noted as dq$_f$ frame, for the FVC. The corrected fundamental voltage reference $v'_{Cfr\alpha\beta}$ in $\alpha\beta$ frame is generated by transforming the reference angle θ_f and the reference amplitude V_f from polar coordinates to $\alpha\beta$ coordinates, and is sent to the voltage-current dual loop.

The sequence diagram shown in Fig. 3 illustrates the transition process from GC to SA mode. In GC mode, each inverter outputs reference active and reactive currents to the utility grid, and the PI controllers in the FVC work without saturation. When a fault occurred in the utility grid, S_u is turned OFF by protection device at $t = t_1$, then the PI controllers in the FVC saturate at $t = t_2$ to restrain the voltage amplitude and frequency in the normal range. Then the inverters work with proportional droop control for power sharing, and seamless transfer is achieved. When the islanding is detected at $t = t_3$, S_i is turned OFF on receiving $IDS = 1$ from at least one inverter using low-bandwidth communication, and the outputs of the PI controllers in the FVC are removed smoothly.

III. Proposed Islanding Detection Method

A. Basic Principle of Synchronized SACS Current Injection

The equivalent circuit of the studied MG at the SACS frequency is shown in Fig. 4. The number of the inverter is indicated in the subscript of the variables. The inverter-side variables (voltages, currents, and impedances) are converted to the PCC side. At the SACS frequency: v_{Cs} is the inverter output voltage, Z_{vs} is the virtual impedance, Z_{ls} is the line impedance, v_{Cs0} is the inverter inner voltage (without the voltage drop of the virtual impedance), Z_{loads} is the PCC load impedance (Y-connected), Z_{gs} is the grid impedance, i_{os} is the inverter output current, v_{PCCs} is the PCC voltage, i_{PCCs} is the current flowing to the PCC from the inverters, i_{gs} is the grid current. Only S_u is shown in Fig. 4, since it determines the transition from GC mode to SA mode.

If the inverters inject SACS without any coordination, there may be large circulating SACS current among the inverters in SA mode. Consequently, some inverters may obtain low impedance amplitudes, and the islanding detection may fail [23]. Therefore, interference among injecting inverters should be avoided. As mentioned in the introduction, the strategy based on synchronized injection is an attractive solution. The synchronization of SACS injection means that i_{PCCs} is equally shared among the inverters. In this case, the equivalent circuit for Inv i is

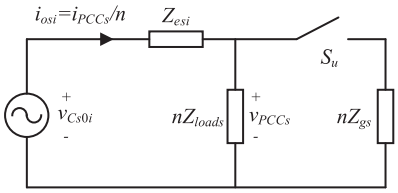

Fig. 5. Equivalent circuit at SACS frequency for Inv i when synchronized SACS injection is achieved.

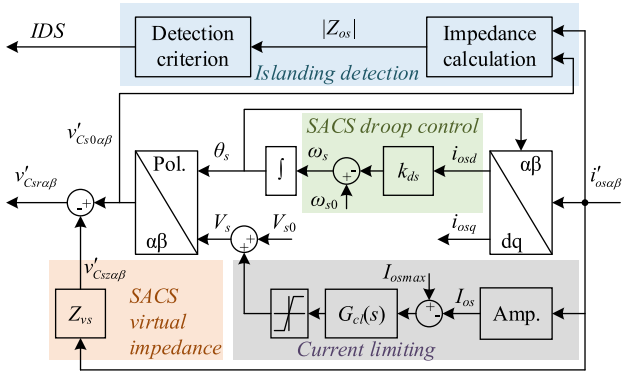

Fig. 6. Block diagram of the proposed islanding detection controller.

shown in Fig. 5, where $Z_{es} = Z_{ls} + Z_{vs}$ is the equivalent line impedance. The impedance Z_{osi} seen from the equivalent inner voltage source $v_{Cs0\,i}$ of Inv i is shown in the following equation:

$$Z_{osi} = Z_{lsi} + Z_{vsi} + nZ_{PCCs} = \begin{cases} Z_{lsi} + Z_{vsi} + \frac{nZ_{loads}Z_{gs}}{Z_{loads}+Z_{gs}}, \text{GC mode} \\ Z_{lsi} + Z_{vsi} + nZ_{loads}, \text{SA mode} \end{cases}. \quad (1)$$

Therefore, islanding can be detected by each inverter in a similar way as in a single-inverter system. Generally, $|Z_{gs}|$ is much smaller than $|Z_{loads}|$. Therefore, after the islanding, $|Z_{osi}|$ will rise significantly. Thus, islanding can be detected by setting an impedance amplitude threshold. The impedance angle can also be detection criterion especially when the PCC load is capacitive [27].

B. Implementation of IDC

The IDC is proposed to achieve islanding detection based on synchronized SACS injection. The block diagram of the IDC is shown in Fig. 6. The extracted $i'_{os\alpha\beta}$ from the MSOGI-PNSC is transformed into the dq frame rotating with the SACS voltage reference angle θ_s, noted as dq$_s$ frame. The IDC use $i'_{os\alpha\beta}$ to generate the corrected SACS voltage reference $v'_{Cs\tau\alpha\beta}$, which includes the voltage drop of SACS virtual impedance $v'_{Csz\alpha\beta}$. The islanding detection signal *IDS* is generated based on the measured impedance seen from the inner voltage source converted to the PCC side using $i'_{os\alpha\beta}$ and $v'_{Cs\tau\alpha\beta}$. The SACS current amplitude is limited in GC mode by the current limiting control.

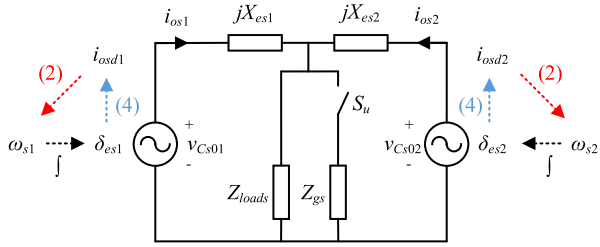

Fig. 7. Equivalent circuit of a system with two inverters at the SACS frequency.

1) Synchronization of SACS Current Injection: To achieve the synchronized SACS current injection, the SACS current should be equally shared among the inverters, which means that i_{osd} and i_{osq} should be equally shared. To share i_{osd}, the i_{osd}-ω_s droop control is established, as shown in (2), where ω_{s0} is the nominal SACS frequency and k_{ds} is the SACS droop coefficient, which are equal for each inverter.

$$\omega_s = \omega_{s0} - k_{ds} i_{osd}. \quad (2)$$

SACS virtual impedance Z_{vs} is implemented to improve the sharing of i_{osq}. The corresponding voltage drop is calculated as in (3). When the equivalent line impedance Z_{es} is the same for each inverter, i_{osq} is equally shared, and perfect synchronization is achieved. If the line impedance is unknown, an identical inductive Z_{vs} can improve the sharing of i_{osq}.

$$\begin{cases} v'_{Csz\alpha} = R_{vs} i'_{os\alpha} - X_{vs} i'_{os\beta} \\ v'_{Csz\beta} = R_{vs} i'_{os\beta} + X_{vs} i'_{os\alpha} \end{cases}. \quad (3)$$

When the equivalent SACS line impedance Z_{es} is inductive, the d-axis SACS current converted to PCC side can be expressed as follows [35]:

$$i_{osd} \approx \frac{V_{PCCs} \sin \delta_{es}}{X_{es}}. \quad (4)$$

In (4), δ_{es} is the equivalent SACS power angle seen from v_{Cs0} in Fig. 5, V_{PCCs} is the SACS voltage amplitude at the PCC, and $X_{es} = X_{ls} + X_{vs}$ is the equivalent SACS line reactance, with X_{ls} being the line reactance and X_{vs} being the virtual reactance.

To explain the sharing of i_{osd} and synchronization of SACS frequency, a system with two inverters is taken as an example. The equivalent circuit at the SACS frequency is shown in Fig. 7. The transformer, together with the initial SACS voltage phase angle of the controller, affects the initial phase of v_{Cs0}, and thus the initial power angle δ_{es}. Ignoring the filtering dynamics, the control of SACS components is independent of fundamental components. Besides, the synchronization process is similar to the conventional current droop control [35]. If initially, there is $i_{osd1} > i_{osd2}$ due to initial values of δ_{es1} and δ_{es2}, according to the SACS droop control (2), there is $\omega_{s1} < \omega_{s2}$, then δ_{es1} decreases, while δ_{es2} increases. From (4), this causes i_{osd1} to decrease, and i_{osd2} to increase, and finally they will become equal. Therefore, in the steady state, ω_s will be the same for each inverter, and i_{osd} will be equally shared.

As for the sharing of i_{osq}, in GC mode, the SACS current amplitude is the same for each inverter due to the SACS current limiting control. Besides, i_{osd} is equally shared by the SACS

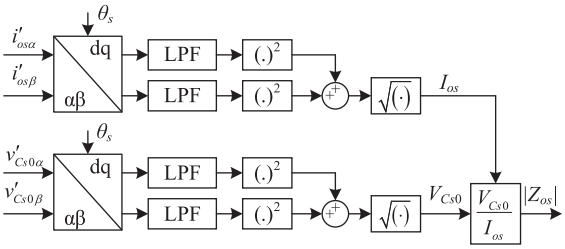

Fig. 8. Block diagram of the impedance calculation in the proposed islanding detection controller.

droop control, as a result, i_{osq} is also equally shared. Therefore, synchronized SACS injection is achieved in GC mode. In SA mode, the SACS voltage amplitude reference V_s equals to the maximal SACS voltage amplitude V_{s0}, and the distribution of i_{osq} depends on the equivalent line impedances of the inverters. A detailed quantitative analysis of the distribution of i_{osq} is given in Section IV.

To summarize, the effectiveness of the proposed method is not affected by winding connection or fundamental components. In contrast, in the existing methods [23], [24], [29], [30], [31], the phase of SACS component is determined by the phase of fundamental voltage, which is affected by fundamental power sharing. Besides, the winding connection may change the relative location between the fundamental voltage and SACS current, which can only be corrected by setting complicated delays according to the winding connection of each inverter [23].

2) Impedance Calculation and Detection Criterion: The impedance amplitude $|Z_{os}|$ is calculated according to Fig. 8, where $i'_{osαβ}$ and $v'_{Cs0αβ}$ are transformed into dq_s frame and then pass through first-order low-pass filters (LPF) with cut-off frequency ω_{LPF} to filter out the noise. Then $|Z_{os}|$ is obtained using the filtered amplitudes I_{os} and V_{Cs0}. Since the SACS injection is synchronized, $|Z_{os}|$ will be close to the theoretical value in (1).

Both the islanding and the grid connection can be detected by comparing $|Z_{os}|$ with corresponding thresholds. A hysteresis is added to improve the robustness of detection, which means islanding detection threshold Z_{t1} is higher than grid connection detection threshold Z_{t2} [27]. In addition, a time threshold T_t is introduced in order to avoid false detection [27]. The flowcharts of the islanding detection and the grid connection detection are shown in Fig. 9. The islanding is confirmed ($IDS = 1$) when the impedance amplitude is larger than Z_{t1} during T_t, and the grid connection is confirmed ($IDS = 0$) when the impedance amplitude is smaller than Z_{t2} during T_t. The IDC can be disabled after the confirmation of the islanding to further improve the voltage quality in SA mode, and can be activated shortly before the grid connection, which is always scheduled.

3) SACS Current Limiting: Using constant SACS voltage reference in GC mode results in large SACS current amplitude, which may violate the restriction on harmonic current. Therefore, a current amplitude limitation block is introduced to control the SACS output current amplitude below a preset value. The SACS current amplitude I_{os} is calculated as in Fig. 8, and is

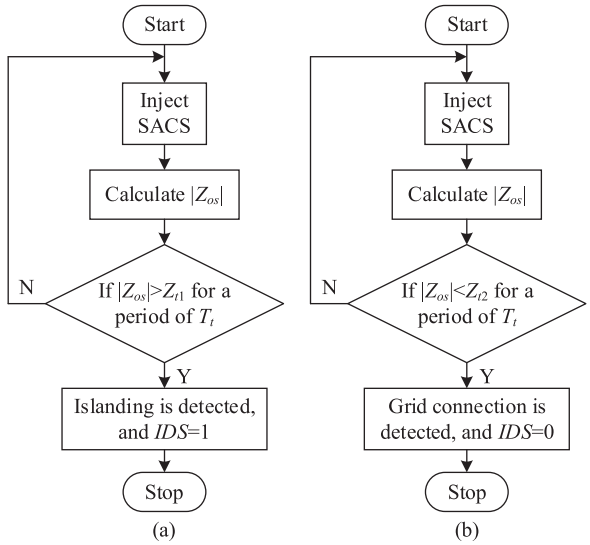

Fig. 9. Flowcharts of (a) islanding detection and (b) grid connection detection.

compared with the preset maximal current amplitude I_{osmax}, and the difference is passed through the PI controller $G_{cl}(s)$, whose upper limit is 0, and lower limit is $-V_{s0}$. In SA mode, since the impedance seen from the output of the inverter is large, I_{os} is lower than the limit value I_{osmax}, and the PI controller saturates at 0, so the SACS voltage amplitude is fixed at V_{s0}. In GC mode, since Z_g is usually very small, I_{os} tends to be larger than I_{osmax}, so the PI controller outputs a negative value to decrease the voltage amplitude V_s. Under the effect of $G_{cl}(s)$, finally I_{os} will be equal to I_{osmax}. Therefore, I_{os} is limited in GC mode.

C. Small-Signal Modeling

Small-signal modeling is essential for parameter design. First, the dq_s-frame linear model of the MSOGI-PNSC is derived in Appendix and obtained in (26).

Second, the small-signal model of the SACS droop control is derived. The SACS power angle δ_{es} is expressed as (5), where ω_{PCCs} is the SACS frequency at the PCC.

$$\delta_{es} = \int (\omega_s - \omega_{PCCs})\, dt. \tag{5}$$

From (4), since the δ_{es} is generally very small, the small-signal relationship in (6) is obtained, where subscript *u* denotes unfiltered variables.

$$\frac{\Delta i_{osdu}}{\Delta \delta_{es}} = \frac{V_{PCCs}}{X_{es}}. \tag{6}$$

In the SACS droop control, the q-axis SACS current is not used, thus it does not influence the d-axis current's dynamics. Therefore, considering the d-to-d transfer function of SACS current extraction of MSOGI-PNSC (26) is enough, which is denoted as $G_{MP}(s)$. Thus, the small-signal equation of d-axis current extraction is obtained

$$\Delta i_{osd}(s) = \mathrm{Re}\left[\mathbf{G_{dq}}(s)\right] \Delta i_{osdu}(s) = G_{MP}(s)\, \Delta i_{osdu}(s). \tag{7}$$

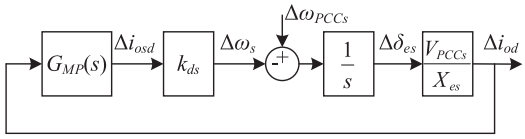

Fig. 10. Small-signal model of the SACS droop control.

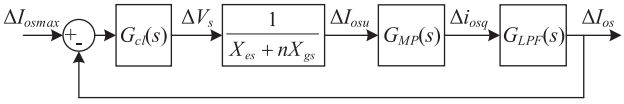

Fig. 11. Small-signal model of the SACS current limiting control.

From (5), the following small-signal relationship can be obtained:

$$\Delta\delta_{es} = \frac{1}{s}\left(\Delta\omega_s - \Delta\omega_{PCCs}\right). \tag{8}$$

The small-signal model of the SACS droop control is shown in Fig. 10. In SA mode, the PCC voltage amplitude V_{PCCs} is close to V_{s0}. In GC mode, due to small Z_{gs} and SACS current limiting control, V_{PCCs} is much smaller than that in SA mode but not zero. Therefore, the SACS synchronization in GC mode is slower than that in SA mode.

Third, the small-signal model of the SACS current limiting control is derived, which is active in GC mode. From Fig. 5 when S_u is turned ON, the SACS current amplitude can be derived as (9) assuming that the synchronization of the SACS current injection is approximately achieved and the load impedance is ignored due to the presence of the grid impedance. Besides, since the line impedance and the grid impedance are mainly inductive, the q-axis current is dominant and we have $I_{osu}{\approx}i_{osqu}$.

$$I_{osu} \approx i_{osqu} \approx \frac{V_s}{X_{es}+nX_{gs}}. \tag{9}$$

The effect of filtering is also considered. Two stages of filtering are present, of which the first stage is MSOGI-PNSC, whose q-to-q transfer function is $G_{MP}(s)$ for q-axis current extraction, and the second stage is the LPF in Fig. 8, whose transfer function is

$$G_{LPF}(s) = \frac{\omega_{LPF}}{s+\omega_{LPF}}. \tag{10}$$

Therefore, the whole calculation process of SACS current amplitude can be approximated as passing the unfiltered q-axis SACS current through two stages of filtering

$$\Delta I_{os} \approx G_{LPF}(s)\,\Delta i_{osq} = G_{LPF}(s)\,G_{MP}(s)\,\Delta I_{osu}. \tag{11}$$

The small-signal relationship related to the current limiting controller is

$$\Delta V_s = G_{cl}(s)\left(\Delta I_{osmax} - \Delta I_{os}\right). \tag{12}$$

By summarizing (9)–(12), the small-signal model of SACS current limiting control is shown in Fig. 11.

IV. Parameter Design

This section focuses on the design of the parameters of the proposed islanding detection method. The design of the voltage-current dual loop is well-established in the literature [34], and is not discussed in this article. The design of the modified droop control in the FVC has been discussed in [13]. The nominal angular frequency ω_{f0} is 100π rad/s, the fundamental nominal phase voltage amplitude V_{f0} is 200 V. In this article, the maximal and minimal d-axis currents are 6 and 0 A. The maximal and minimal q-axis currents are 3 and -3 A. The reference d-axis current i_{ofrd} is 3 A, and the reference q-axis current i_{ofrq} is 0 A. The d-axis droop coefficient k_{df} is set as 0.21, the q-axis droop coefficient k_{qf} is set as 3.33. The limit values in the modified droop control are set as $\pm$ 0.4π rad/s and $\pm$ 10 V, so that in the worst case after the islanding, the maximal deviations of frequency and voltage are $\pm$ 0.4 Hz and $\pm$ 20 V ($\pm$ 10%), respectively, within the maximal deviations for continuous operation defined in IEEE 1547 standard [36].

A. Frequency and Amplitudes of SACS

Since the synchronization of injection is independent from the fundamental output voltage, theoretically the selection of the nominal SACS frequency is not restricted to integer harmonic frequencies as in the conventional method [23]. However, the limitations at interharmonics and subharmonics are generally more rigorous than those at integer harmonics [37]. In this article, the nominal SACS frequency ω_{s0} is the fourth harmonic frequency 400π rad/s, which is normally not present in the original three-phase system [34].

The maximal SACS phase voltage amplitude V_{s0} should be designed considering the trade-off between the power quality and the accuracy of impedance measurement. In this article, V_{s0} is 5 V, which is 0.025 p.u. and satisfies the IEEE standard which limits individual harmonics within 5% [37].

The maximal SACS current amplitude I_{osmax} should not exceed the maximal value defined in the grid code. The limit value the fourth harmonic current is 2% of the rated current I_{rated} of the DG unit [36], as shown in the following equation:

$$I_{osmax} < 0.02 I_{rated}. \tag{13}$$

On the other hand, I_{osmax} should not be too low to avoid low accuracy of impedance measurement. In this article, I_{rated} is 15 A, and I_{osmax} is set to 0.2 A.

B. Control Parameters

The impact of key parameters on the system dynamic performance is studied as follows.

1) Gains of MSOGI k_{SOGIf} *and* k_{SOGIs}*:* The gains in MSOGI satisfy that $k_{SOGIs} = k_{SOGIf}/4$, in order to obtain the same bandwidth of both extraction channels. The design of k_{SOGIf} faces the trade-off between filtering and dynamics of MSOGI-PNSC. Besides, k_{SOGIf} also affects the dynamics of other control loops. In this article, $k_{SOGIf} = 1.41$ is selected, which is the recommended value in [33] to achieve good dynamics of MSOGI-PNSC.

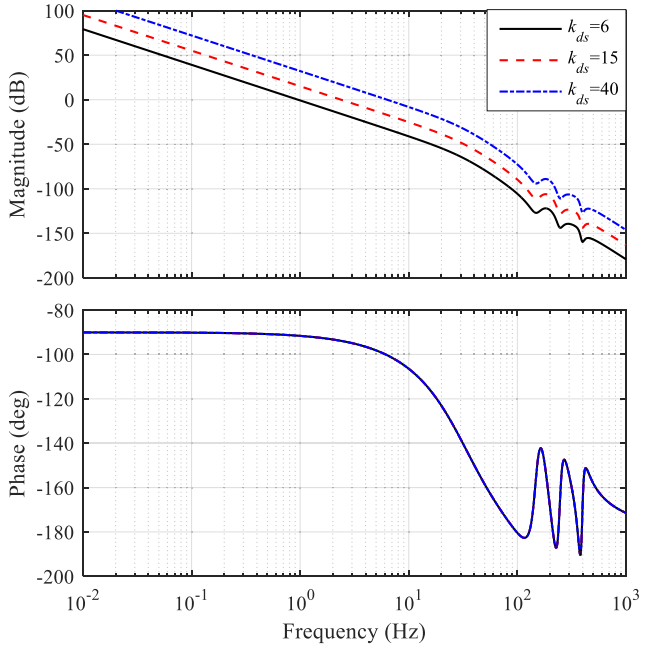

Fig. 12. Open-loop bode plots of SACS droop control with different k_{ds}.

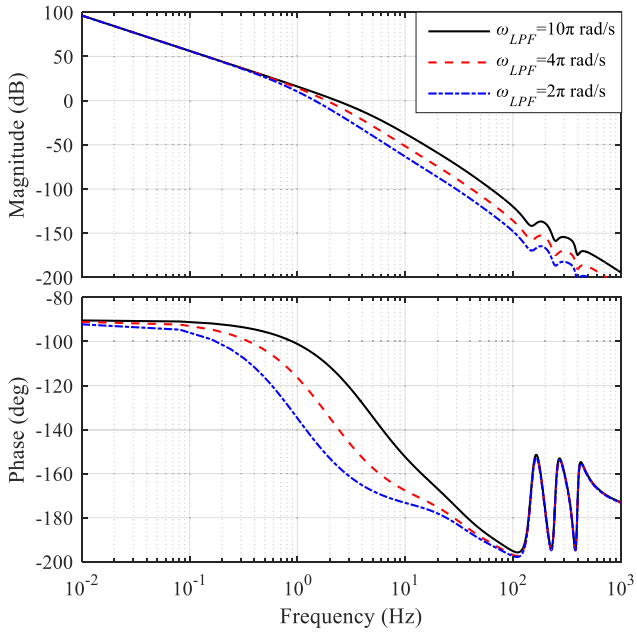

Fig. 13. Open-loop bode plots of SACS current limiting control with different ω_{LPF}.

2) SACS Droop Coefficient k_{ds}*:* In the SACS droop control, the key parameters that affect system dynamic behavior include k_{ds} and k_{SOGIf}. By fixing $k_{SOGIf} = 1.41$, the influence of k_{ds} can be investigated. The SACS frequency deviation is determined by k_{ds}, and when k_{ds} is too large, the SACS can no longer be regarded as the fourth harmonic. The SA mode is considered. Knowing $V_s = 5$ V, V_{PCCs}≈5 V, X_{es}≈5 Ω, and $k_{SOGIf} = 1.41$, based on Fig. 10, the open-loop bode plots of the SACS droop control with different k_{ds} can be obtained and are shown in Fig. 12. As can be seen, larger k_{ds} leads to larger crossover frequency and smaller phase margin. Therefore, larger k_{ds} will increase the SACS synchronization speed at the cost of larger SACS frequency deviation. The requirement on SACS synchronization speed is not high, since the GC mode generally provides enough time for SACS synchronization. In this article, $k_{ds} = 6$ is selected, so that the SACS frequency deviation is less than $k_{ds}I_{osmax} = 0.6$ Hz. With this design, it can be observed from Fig. 12 that the crossover frequency is 0.955 Hz and the phase margin is 88.45°.

3) Cut-Off Frequency of LPF ω_{LPF}*:* In the SACS current limiting control, the key parameters that affect the SACS current limiting control are parameters of $G_{cl}(s)$, k_{SOGIf}, and ω_{LPF}. $G_{cl}(s)$ is set as $k_p(1+200/s)$, so that its corner frequency is around the cut-off frequency of $G_{MP}(s)$. The influence of ω_{LPF} is investigated. X_{gs} is ignored for the design since it is generally very small. Knowing $V_s = 5$ V, V_{PCCs}≈5 V, X_{es}≈5 Ω, $k_{SOGIf} =$ 1.41, and $k_p = 0.4$, based on Fig. 11, the open-loop bode plots of the SACS current limiting control with different ω_{LPF} are shown in Fig. 13. Smaller ω_{LPF} improves the filtering performance of I_{os}, but decreases both the phase margin and the crossover frequency according to Fig. 13, so that the response time will be longer and the dynamics tend to be oscillatory. Besides, it can be predicted that larger k_p leads to larger crossover frequency and less phase margin. In this article, ω_{LPF} is selected to 10π rad/s, and k_p is 0.4. In this case, the crossover frequency is 2.31 Hz, and the phase margin is 65.6°.

To summarize, larger k_{SOGIf} leads to faster signal extraction but poorer filtering. Larger k_{ds} results in faster SACS synchronization, but the SACS frequency deviates more. Larger k_p in G_{cl}(s) increase the response speed of current limiting control at the cost of phase margin. Larger ω_{LPF} improves the filtering of I_{os} but deteriorates the dynamics.

C. Threshold Setting

When the equivalent line impedances are equal for each inverter, perfect synchronization of injection is achieved, and the measured impedance amplitudes correspond to (1), which are the same for each inverter. Therefore, the threshold can be the same for every inverter. Based on the ranges of Z_{loads}, Z_{gs}, and Z_{es}, the range of amplitude threshold can be determined, considering that the islanding should still be detected with the smallest Z_{loads} (that is, largest PCC load) in SA mode. Then the impedance thresholds Z_{t1} and Z_{t2} can be designed as shown in (14). The thresholds are related to n, which normally does not change quickly, and can be regarded as fixed value or be transmitted by communication with low bandwidth.

$$|nZ_{gs} + Z_{es}| < Z_{t2} < Z_{t1} < \min|nZ_{loads} + Z_{es}|. \quad (14)$$

The time threshold T_t is set according to the level of noise and transients. In this article, T_t is set to be 1 s, which is larger than necessary to show more clearly the whole process of islanding detection.

If the line impedances are not equal, by using some non-invasive methods [38], [39], [40], the line impedances can be

measured, and SACS virtual impedance can be set accordingly to achieve perfect synchronization of injection. If it is not feasible to measure line impedances, a same inductive Z_{vs} can be implemented for each inverter to reduce the relative difference among equivalent line impedances. However, the measured impedances will still be different. In the following, the influence of unequal equivalent line impedances on impedance measurement is analyzed.

In GC mode, since both i_{osd} and i_{osq} are equally shared, assuming that δ_{es1}, δ_{es2} are close to each other, the SACS currents flowing from inverters to PCC can be considered to be almost identical, so (1) is still almost accurate in GC mode when the line impedances are different. Then the deviation of measured impedance is the deviation of equivalent line impedance, which is generally much smaller than the load impedance and does not affect islanding detection.

In SA mode, to simplify the discussion, a system containing two inverters is investigated. In the steady state, the d-axis current is equally shared between both inverters by the SACS droop control, while the steady-state q-axis currents are shown in (15) [35], where the subscript *i* represents 1 or 2.

$$I_{osqi} = \frac{R_{esi} V_{PCCs} \sin \delta_{esi} - X_{esi} \left(V_{s0} - V_{PCCs} \cos \delta_{esi}\right)}{R_{esi}^2 + X_{esi}^2}. \tag{15}$$

The line impedances are assumed to be purely inductive at the SACS frequency. Besides, since in SA mode, the PCC load impedance is generally much larger than the line impedances, δ_{es1} and δ_{es2} are very small. Therefore, the following approximation is obtained from (15):

$$I_{osqi} \approx \frac{V_{PCCs} - V_{s0}}{X_{esi}}. \tag{16}$$

Therefore, the sharing of q-axis SACS current is inversely proportional to the equivalent line impedance. Set the coefficient of line impedance mismatch *m*, which means that the equivalent line impedance of Inv 1 is $(1+m)Z_{es\text{-}av}$ and the equivalent line impedance of Inv 2 is $(1-m)Z_{es\text{-}av}$, where $Z_{es\text{-}av}$ is the average value of the equivalent line impedances. Suppose that I_{osdt} and I_{osqt} are total steady-state dq-axis currents, we have

$$\begin{cases} I_{osd1} = I_{osd2} = \frac{1}{2} I_{osdt} \\ I_{osq1} = \frac{1-m}{2} I_{osqt}, I_{osq2} = \frac{1+m}{2} I_{osqt} \end{cases}. \tag{17}$$

Set $I_{osqt} = n_r I_{osdt}$, where n_r represents the ratio of the reactive component to the active component in the SACS current and it depends on the power factor of the load. Then the magnitudes of the measured impedances are

$$\begin{aligned} |Z_{os1}| &= \frac{V_{s0}}{I_{osdt} \sqrt{\left(\frac{1}{2}\right)^2 + \left(\frac{1-m}{2} n_r\right)^2}} \\ |Z_{os2}| &= \frac{V_{s0}}{I_{osdt} \sqrt{\left(\frac{1}{2}\right)^2 + \left(\frac{1+m}{2} n_r\right)^2}}. \end{aligned} \tag{18}$$

The approximative expressions of relative magnitude variations of measured impedances are shown in (19), where Z_{os0} is the measured impedance when equivalent line impedances of both inverters are identical, i.e., $m = 0$.

$$\begin{aligned} K_1 &= \frac{|Z_{os1}|}{|Z_{os0}|} = \sqrt{\frac{1+n_r^2}{1+\left[(1-m)\, n_r\right]^2}} \\ K_2 &= \frac{|Z_{os2}|}{|Z_{os0}|} = \sqrt{\frac{1+n_r^2}{1+\left[(1+m)\, n_r\right]^2}}. \end{aligned} \tag{19}$$

From (19), larger *m* leads to larger deviations from $|Z_{os0}|$. Besides, the influence of *m* on K_1 and K_2 is positively correlative with n_r. If the PCC load is parallel RL load, since the impedance of inductance branch increases in high frequency range, n_r tends to be small. In the special case where the inductance is infinite, $n_r = 0$ and $K_1 = K_2 = 1$, therefore, even if the line impedances change, the measured impedances remain the same. If the PCC load is parallel RC load, n_r might be large, and thus K_1 and K_2 might deviate significantly from 1. Besides, the measured impedance amplitudes in SA mode might be small. In this case, the criterion based on impedance amplitude may fail. However, the SACS impedance angle becomes negative in case of islanding [27], which facilitates the islanding detection.

In the rest of this article, the PCC load is assumed to be parallel RL load, while other types of inductive load at the SACS frequency can be transformed into parallel RL load. Fig. 14 shows the variation of K_1 and K_2 with *m* under $n_r = 1/4$ and $n_r = 1/8$, where the solid lines represent the results of the approximation (19), and the dashed lines with symbols are simulation results.

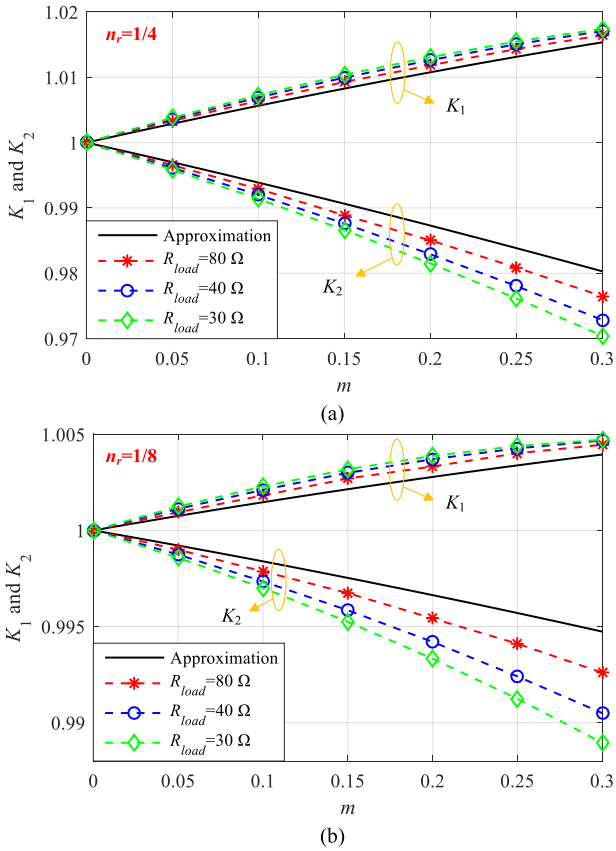

Fig. 14. Variation of K_1 and K_2 with *m* under (a) $n_r = 1/4$ and (b) $n_r = 1/8$.

TABLE II
SIMULATION AND EXPERIMENTAL PARAMETERS

Symbol	Description	Value
V_{f0}	Nominal fundamental voltage (V)	200
V_{s0}	Nominal SACS voltage (V)	5
ω_{f0}	Nominal fundamental frequency (rad/s)	100π
ω_{s0}	Nominal SACS frequency (rad/s)	400π
k_{ds}	SACS droop coefficient (rad/s/A)	6
k_{SOGIf}	Gain of the MSOGI	1.41
ω_{LPF}	Cut-off frequency of the LPF (rad/s)	10π
I_{osmax}	Maximal SACS current amplitude (A)	0.2
Z_l	Line impedance (mH+Ω)	4+1
Z_{t1}	Impedance threshold for islanding detection (Ω)	30
Z_{t2}	Impedance threshold for connection detection (Ω)	10
T_t	Time threshold (s)	1

In the simulations, the parameters in Table II are used except that Z_l is 4 mH in series with 0.02 Ω when $m = 0$. SACS virtual impedance is not implemented. When the resistance branch R_{load} changes, the inductance varies accordingly to maintain the fixed n_r. It can be seen that the simulation results are close to the approximation especially when R_{load} is large, since larger R_{load} leads to smaller power angle, making the assumption of small power angle more valid. In Fig. 14, the deviations of K_1 and K_2 from 1 do not exceed 5% even with $m = 0.3$. Therefore, for RL load, (14) can still be used to determine the detection thresholds when there is considerable mismatch among the line impedances of the inverters.

V. SIMULATION AND EXPERIMENTAL RESULTS

The proposed method is validated through simulation and experimental results. The default main parameters are listed in Table II. Note that the nominal voltage amplitudes in Table II are of phase voltages in their corresponding dq frame.

A. Simulation

Simulations are carried out in PSCAD to validate the effectiveness of the proposed method.

1) Performance Verification: In the first simulation, a MG system with three parallel inverters is tested. Inv 1 and 3 are equipped with transformers, while Inv 2 is without transformer. The transformer of Inv 1 has turns ratio 1:1.1, and the winding connection is Dy1. The transformer of Inv 3 has turns ratio 1:1, and the winding connection is Dy11. The grid impedance Z_g is 1 mH.

Before $t = 6$ s, the MG works under GC mode, and a resistive load Z_{load} of 15 Ω is connected at the PCC. At $t = 6$ s, the islanding occurs. At $t = 8$ s, Z_{load} changes to 30 Ω.

Fig. 15 shows the related waveforms. From Fig. 15(a), the amplitudes of measured impedance are below Z_{t2} before $t = 6$ s, and rise beyond Z_{t1} within around 51 ms after islanding. Since the line impedances are the same, the steady-state $|Z_{os}|$ is identical for each inverter. After the load change at t = 8 s, the impedance amplitudes rise uniformly from around 45 Ω to around 90 Ω, consistent with the theoretical values of (1).

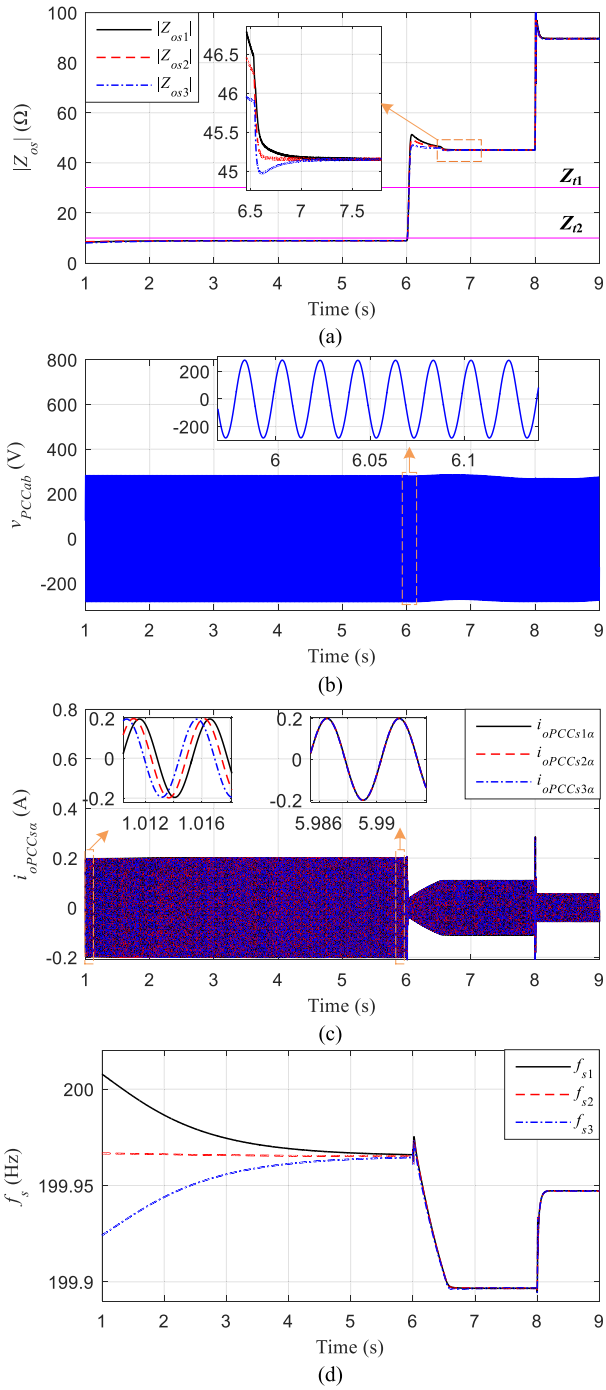

Fig. 15. Simulation waveforms of (a) amplitudes of measured impedance, (b) PCC line voltage, (c) PCC side α-axis output SACS currents, and (d) SACS frequencies in the MG with the proposed islanding detection method.

From Fig. 15(b), the PCC voltage is within normal range before and after islanding, and the seamless transfer is observed when islanding occurs. Note that the envelope of v_{PCCab} is in the normal range but is slightly oscillating at a low frequency after the islanding, because the SACS voltage amplitude rises and the

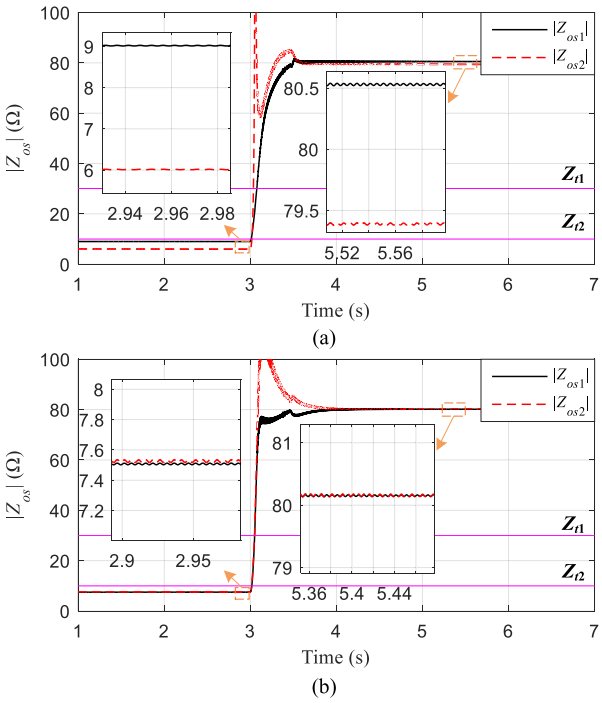

Fig. 16. Simulation waveforms of measured impedance with $n_r = 1/8$ and $R_{load} = 40$ (a) without SACS virtual impedances and (b) with SACS virtual impedances.

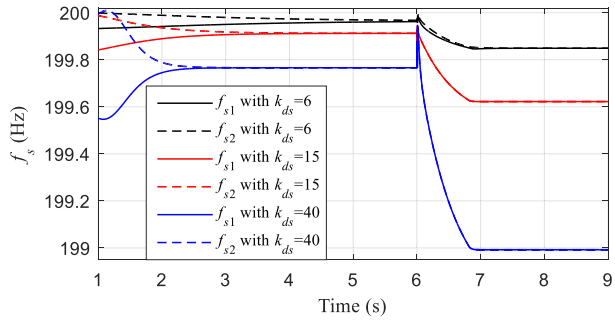

Fig. 17. Simulation waveforms of f_{s1} and f_{s2} with different k_{ds} in case of initial SACS phase difference.

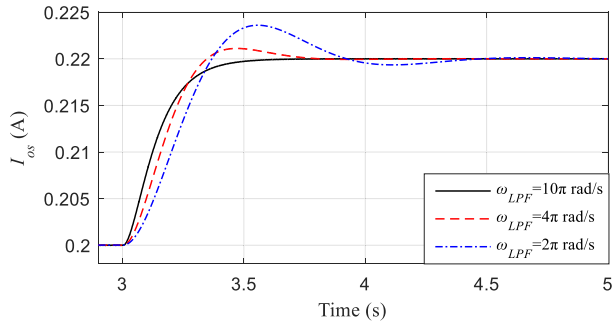

Fig. 18. Simulation waveforms of I_{os} under perturbation in I_{osmax} with different ω_{LPF}.

SACS frequency is not strictly integer times of the fundamental frequency.

From Fig. 15(c), in GC mode, the amplitudes of SACS current of the inverters are well-limited at I_{osmax}. At the beginning, the PCC-side SACS currents are not synchronized due to different initial conditions, but are almost completely synchronized before $t = 6$ s. After the islanding, the SACS current amplitudes decrease suddenly due to the increase in PCC impedance, but then increase gradually to a constant value, since the SACS voltage amplitude reference V_s increases after the islanding until the saturation of the current limiting controller.

From Fig. 15(d), at the beginning, there are differences among the SACS frequencies ($\omega_s = 2\pi f_s$). After several seconds, the SACS frequencies become identical, which marks the equal sharing of i_{osd}, and the synchronization is achieved. Besides, after the islanding, the SACS frequencies remain almost the same in both transient and steady states, showing that the synchronized injection is maintained.

2) Influence of Equivalent Line Impedances: Simulations are done to study the influence of equivalent line impedances during the islanding detection process. The parameters are the same as in Fig. 14(b) when $n_r = 1/8$, $R_{load} = 40\,\Omega$, and $m = 0.3$. Islanding occurs at $t = 3$ s.

Fig. 16(a) shows the measured impedances when the SACS virtual impedances are not implemented. As can be seen, with unequal line impedances, the measured impedances deviate from each other, but islanding can still be detected. The results in SA mode correspond to the points on the blue dashed lines in Fig. 14(b) with $n_r = 1/8$, $R_{load} = 40\ \Omega$, and $m = 0.3$. The difference of measured impedances in GC mode is around 3 Ω, which is approximately the difference of line impedance 3.02 Ω, consistent with the previous analysis.

Fig. 16(b) shows the measured impedances when SACS virtual impedances are implemented to make the equivalent line impedances equal to $Z_{es\text{-}av}$. As can be seen, after implementing the SACS virtual impedances, despite some transients, the measured impedances are equal in the steady states of GC mode and SA mode, marking the perfect synchronization of injection.

3) Parameter Variation: To verify the impact of k_{ds} on the SACS droop control, a system with two inverters is simulated. At the beginning, the phase of the SACS voltage of Inv 2 lags that of Inv 1 by 60°. The PCC load is pure resistive load 15 Ω. Islanding occurs at $t = 6$ s. The waveforms of f_{s1} and f_{s2} with different k_{ds} are shown in Fig. 17. As can be seen, larger k_{ds} leads to faster synchronization speed of SACS but also larger SACS frequency deviation.

Meanwhile, to verify the influence of ω_{LPF} on the SACS current limiting control, a system with two inverters in GC mode is simulated. The PCC load is pure resistive load 15 Ω. At $t = 3$ s, I_{osmax} increases from 0.2 to 0.22 A, thus producing a perturbation in the input of the current limiting control loop. The waveforms of I_{os} of Inv 1 under different ω_{LPF} are shown in Fig. 18. As can be seen, lower ω_{LPF} leads to slower transients and larger overshoot, which is consistent with the previous analysis based on the bode plots in Fig. 13.

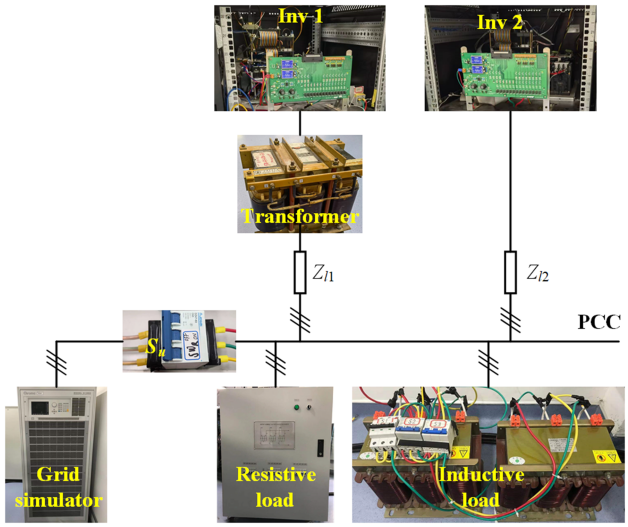

Fig. 19. Experimental platform.

B. Experimental Results

The effectiveness of the proposed method is verified on the MG test platform. The system contains two parallel three-phase inverters of type MWINV-9R144 with LC filters, resistive and inductive loads, and grid simulator of type 61860 from Chroma, with the same topology in Fig. 1. The algorithm is implemented on DSP TMS320F28335 from Texas Instruments in each inverter. A photo of the experimental platform is shown in Fig. 19. The main parameters are listed in Table II. Inv 1 is equipped with a transformer in Cases 2 and 3 in the method comparison part, in other cases Inv 1 is directly connected to Z_{l1} without transformer.

1) Performance Verification: To verify the correctness of the impedance measurement, the proposed islanding detection method is tested with different PCC load impedances Z_{load}, which are 20, 26.67, and 26.67 Ω in parallel with 50 mH. No transformer is used. Fig. 20 shows the resulting waveforms of $|Z_{os}|$ of both inverters, the PCC line voltage v_{PCCab} and grid current i_{ga}. In GC mode, both $|Z_{os1}|$ and $|Z_{os2}|$ are around 8 Ω. After the islanding, which is indicated by a sudden decrease to zero of i_{ga}, the PCC voltage is in the normal range by the seamless transfer strategy, and both $|Z_{os1}|$ and $|Z_{os2}|$ increase significantly and exceed the threshold Z_{t1}. The measured impedance amplitudes are close to the theoretical values calculated from (1), which are 41.3, 54.6, and 52.2 Ω, respectively. The steady-state errors might be due to inaccurate line impedances. The impedance measurement shows some fluctuation due to noise in the current measurement, since the SACS current is relatively small in SA mode. Despite some steady-state error and fluctuation in the impedance measurement, the islanding is successfully detected in all the three cases. After that the islanding is confirmed, the outputs of the limiters are removed, which caused some transients in the impedance measurement.

To verify the effectiveness of the SACS current limiting control, the performances of the proposed method with and without current limiting control are compared. When the current limiting control is disabled, a fixed SACS voltage amplitude

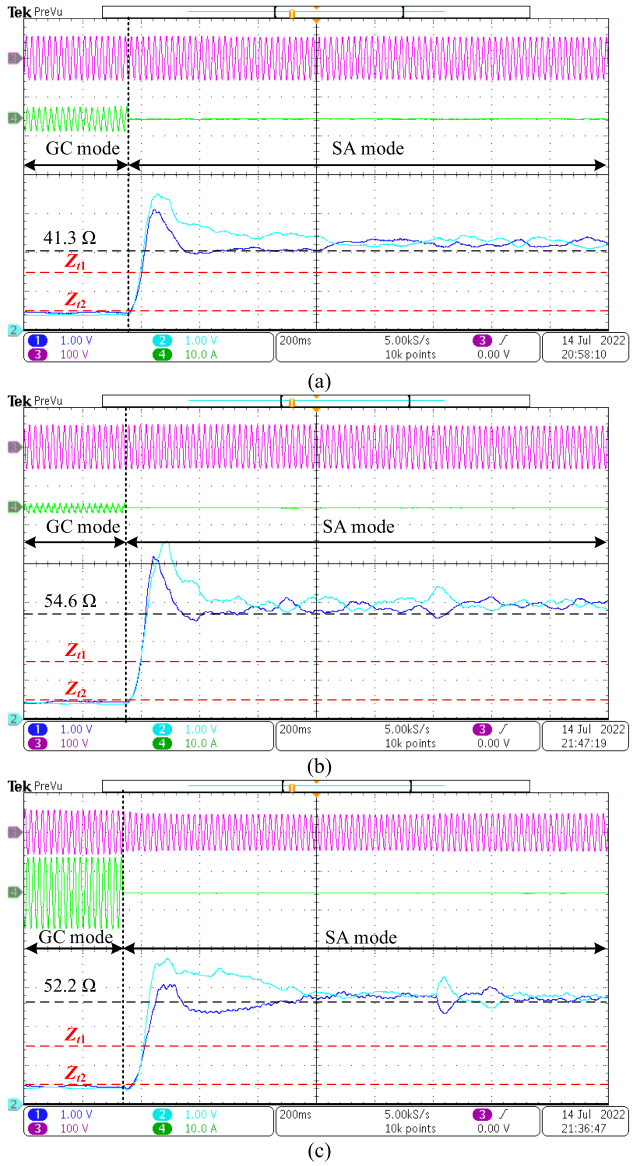

Fig. 20. Experimental waveforms of the MG with the proposed islanding detection method when the PCC load Z_{load} is (a) 20 Ω, (b) 26.67 Ω, and (c) 26.67 Ω + 50 mH, respectively: CH1, $|Z_{os1}|$, 20 Ω/div; CH2, $|Z_{os2}|$, 20 Ω/div; CH3, v_{PCCab}, 500 V/div; CH 4, i_{ga}, 10 A/div.

(5 V) is adopted. Fig. 21 shows the resulting waveforms of I_{os} of both inverters and the grid current i_{ga}. As can be seen, when there is no SACS current limiting, the SACS current amplitude I_{os} of each inverter is around 0.63 A, and i_{ga} is significantly distorted. If the proposed current limiting method is adopted, I_{os} of both inverters is limited to the defined maximal SACS current amplitude I_{osmax}, which is 0.2 A, and i_{ga} is less distorted.

The plug-and-play feature of the proposed method is tested. Since in SA mode, the islanding detection can be disabled, the plug-and-play feature is tested in GC mode. At first, Inv 1 is working in GC mode and Inv 2 is not connected to the system. Then Inv 2 is plugged into the MG after synchronizing its fundamental output voltage with the PCC voltage. The PCC load is 20 Ω. Fig. 22 shows the resulting waveforms of $|Z_{os}|$ of both

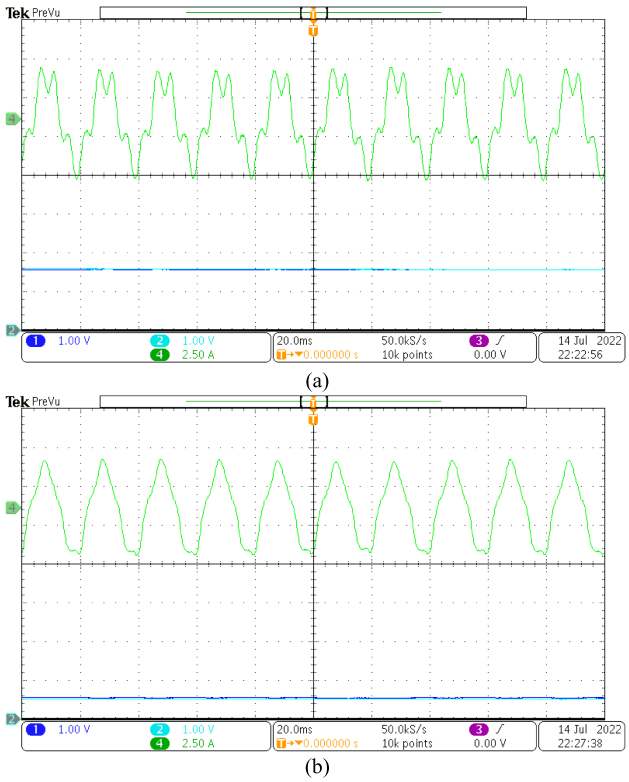

Fig. 21. Experimental waveforms of the grid current and the SACS current amplitude in GC mode (a) without SACS current limiting, and (b) with SACS current limiting: CH1, I_{os1}, 0.4 A/div; CH2, I_{os2}, 0.4 A/div; CH4, i_{ga}, 2.5 A/div.

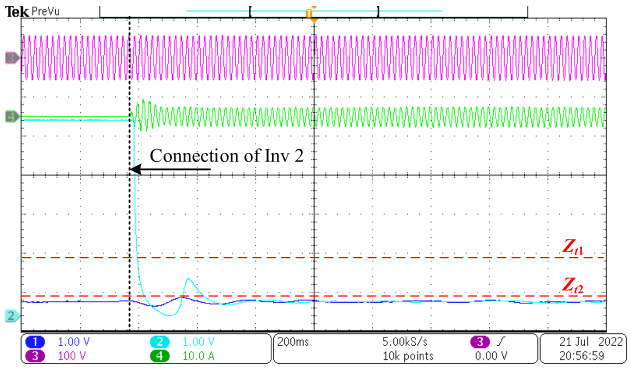

Fig. 22. Experimental waveforms when Inv 2 is plugged into the MG in GC mode: CH1, $|Z_{os1}|$, 20 Ω/div; CH2, $|Z_{os2}|$, 20 Ω/div; CH3, v_{PCCab}, 500 V/div; CH 4, i_{o2}, 10 A/div.

inverters, the PCC line voltage v_{PCCab} and the output current of Inv 2 i_{o2}. At the beginning, $|Z_{os2}|$ is above 100 Ω (beyond the digital-to-analog converter's output range 5 V) because no load is connected to Inv 2, and $|Z_{os1}|$ is below Z_{t2}. After the connection of Inv 2, which is indicated by an increase in i_{o2} from zero, $|Z_{os2}|$ decreases to about 8 Ω, below Z_{t2}, so the grid connection can be detected by Inv 2, while $|Z_{os1}|$ almost remains unchanged. Therefore, any new inverter can be plugged into the MG without modification of the existing equipment, and the islanding detection of other inverters is not affected, showing the plug-and-play feature of the proposed islanding detection method.

2) Comparison With Existing Method: The proposed islanding detection is compared with the conventional method used in [23] and [30], where the current control is implemented for each GFL inverter, and the phase of the SACS inductor current is four times of the phase of fundamental output voltage to achieve synchronization. The fundamental inductor current reference is 3.5 A d-axis current, while the SACS inductor current reference is 0.4 A d-axis current. Some modifications are made to the original control diagram in Fig. 10 [30]: 1) to improve the phase tracking, the output voltage passes through an MSOGI-PNSC, and the extracted fundamental positive sequence component is sent to a synchronous rotating frame-PLL (SRF-PLL); 2) another MSOGI-PNSC is used to extract SACS positive sequence inductor current, and the measured impedance is calculated from the extracted SACS output voltage and the extracted SACS output current; 3) In order to limit the frequency deviation and to maintain the stable operation after the islanding, the estimated frequency of the SRF-PLL is limited in the range from 45 to 55 Hz.

The PCC load is 20 Ω. According to (1), the measured impedance of each inverter is 41.3 Ω when the synchronized SACS current injection is achieved. Three cases are tested:

Case 1: the conventional method is implemented, and no transformer is used.

Case 2: the conventional method is implemented, and Inv 1 is equipped with a transformer. The turns ratio is 1:1, the winding connection is Dy11, with the PCC side being the primary side. The formula of delay setting in [23] is not adopted since the information on winding connections of transformers is assumed to be unknown by the inverters.

Case 3: the proposed method is implemented, and Inv 1 is equipped with the same transformer as in Case 2.

Fig. 23 shows the resulting waveforms of $|Z_{os}|$ of both inverters, the PCC line voltage v_{PCCab} and the grid current i_{ga}. In Case 1, $|Z_{os1}|$ and $|Z_{os2}|$ are around 40 Ω after islanding, above Z_{t1}, so the islanding can be detected. However, after islanding, the amplitude of v_{PCCab} decreases significantly below the allowed value (−10%), and $|Z_{os1}|$ and $|Z_{os2}|$ show large fluctuation even if the amplitude of injected SACS current (0.4 A) is larger than that in the proposed method. It can be further verified that the system tends to be unstable if the estimated frequency of the SRF-PLL is not limited, making the verification of the islanding detection difficult. To further improve the voltage quality after the islanding, the seamless transfer strategies in [7] and [8] might be used, which do not rely on islanding detection, but the outer voltage loop may interact with the harmonic injection, and this issue has not been discussed in the existing literature.

In Case 2, $|Z_{os1}|$ and $|Z_{os2}|$ show obvious difference after islanding, and both are generally below the detection threshold Z_{t1}, thus the islanding detection fails. Besides, large voltage transients and degraded voltage quality are observed again.

In Case 3, after the islanding, $|Z_{os1}|$ and $|Z_{os2}|$ are around the theoretical value. Therefore, the effectiveness of the proposed method is not affected by transformers. Besides, because of the

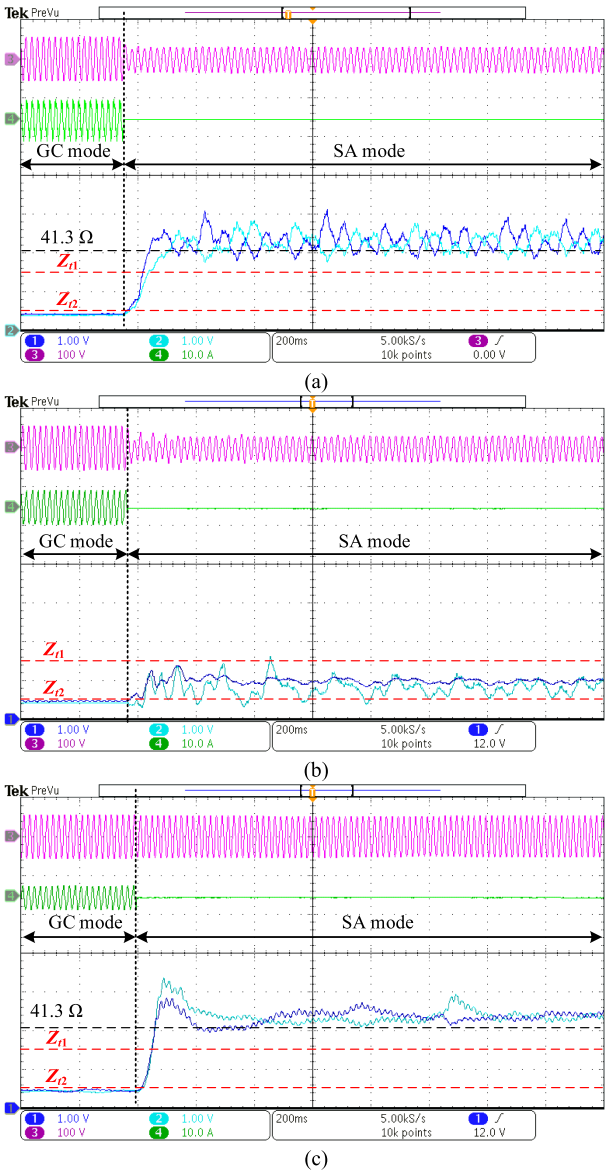

Fig. 23. Experimental waveforms of the MG with the method for comparison. (a) Case 1, (b) Case 2, and (c) Case 3: CH1, $|Z_{os1}|$, 20 Ω/div; CH2, $|Z_{os2}|$, 20 Ω/div; CH3, V_{PCCab}, 500 V/div; CH 4, i_{ga}, 10 A/div.

incorporated seamless transfer strategy, the voltage quality is maintained in SA mode.

VI. Conclusion

An islanding detection method based on synchronized SACS current injection for the MG comprised of GFM inverters with seamless transfer capabilities has been presented in this article. The proposed method achieves synchronization of SACS injection without being affected by winding connections of grid-side transformers or fundamental components. Besides, the proposed method reduces the impact on the grid current quality by using SACS current limiting control. In addition, the control scheme is peer-to-peer and enables plug-and-play functionality. The effectiveness and advantages of the proposed method have been validated through simulation and experimental results. The concept of the proposed method can also be applied in single-phase MGs.

Appendix

Linear Model of MSOGI-PNSC in dq_s Frame

To simplify the discussion, and since the frequency adaptation is not designed to be very fast, the resonant frequencies of MSOGI are assumed to be the nominal frequencies. Then the equation of SACS current extraction of the MSOGI is

$$\begin{bmatrix} i'_{os\alpha x} \\ qi'_{os\alpha x} \\ i'_{os\beta x} \\ qi'_{os\beta x} \end{bmatrix} = \begin{bmatrix} G_d(s) & 0 \\ G_q(s) & 0 \\ 0 & G_d(s) \\ 0 & G_q(s) \end{bmatrix} \begin{bmatrix} i'_{o\alpha} \\ i'_{o\beta} \end{bmatrix} \tag{20}$$

where $G_d(s)$ and $G_q(s)$ are the in-phase and quadrature transfer functions of the SACS extraction channel, expressed as follows:

$$\begin{cases} G_d(s) = \dfrac{\frac{k_{SOGIs}\omega_{s0}s}{s^2+\omega_{s0}^2}}{1+\frac{k_{SOGIs}\omega_{s0}s}{s^2+\omega_{s0}^2}+\frac{k_{SOGIf}\omega_{f0}s}{s^2+\omega_{f0}^2}} \\ G_q(s) = \dfrac{\frac{k_{SOGIs}\omega_{s0}^2}{s^2+\omega_{s0}^2}}{1+\frac{k_{SOGIs}\omega_{s0}s}{s^2+\omega_{s0}^2}+\frac{k_{SOGIf}\omega_{f0}s}{s^2+\omega_{f0}^2}} \end{cases}. \tag{21}$$

The equation of the PNSC is

$$\begin{bmatrix} i'_{os\alpha} \\ i'_{os\beta} \end{bmatrix} = \begin{bmatrix} \frac{1}{2} & 0 & 0 & -\frac{1}{2} \\ 0 & \frac{1}{2} & \frac{1}{2} & 0 \end{bmatrix} \begin{bmatrix} i'_{os\alpha x} \\ qi'_{os\alpha x} \\ i'_{os\beta x} \\ qi'_{os\beta x} \end{bmatrix}. \tag{22}$$

By combining (20) and (22), the following is obtained:

$$\begin{bmatrix} i'_{os\alpha} \\ i'_{os\beta} \end{bmatrix} = \frac{1}{2} \begin{bmatrix} G_d(s) & -G_q(s) \\ G_q(s) & G_d(s) \end{bmatrix} \begin{bmatrix} i'_{o\alpha} \\ i'_{o\beta} \end{bmatrix} \tag{23}$$

which can be expressed in complex $\alpha\beta$ frame

$$\mathbf{i'_{os\alpha\beta}} = \frac{1}{2}\left[G_d(s) + jG_q(s)\right]\mathbf{i'_{o\alpha\beta}}. \tag{24}$$

Its form in complex dq frame is obtained by frequency shift

$$\mathbf{i'_{osdq}} = \underbrace{\frac{1}{2}\left[G_d(s+j\omega_{s0}) + jG_q(s+j\omega_{s0})\right]}_{\mathbf{G_{dq}}(s)}\mathbf{i'_{odq}}. \tag{25}$$

By transforming (25) into dq_s frame, the following relationship is obtained:

$$i'_{osdq} = \begin{bmatrix} \mathrm{Re}\left[\mathbf{G_{dq}}(s)\right] & -\mathrm{Im}\left[\mathbf{G_{dq}}(s)\right] \\ \mathrm{Im}\left[\mathbf{G_{dq}}(s)\right] & \mathrm{Re}\left[\mathbf{G_{dq}}(s)\right] \end{bmatrix} i'_{odq}. \tag{26}$$

References

[1] M. Gao, M. Chen, B. Zhao, B. Li, and Z. Qian, "Design of control system for smooth mode-transfer of grid-tied mode and islanding mode in microgrid," *IEEE Trans. Power Electron.*, vol. 35, no. 6, pp. 6419–6435, Jun. 2020.

[2] R. H. Lasseter and P. Paigi, "Microgrid: A conceptual solution," in *Proc. IEEE 35th Annu. Power Electron. Specialists Conf.*, 2004, pp. 4285–4290.

[3] J. Rocabert, A. Luna, F. Blaabjerg, and P. Rodríguez, "Control of power converters in AC microgrids," *IEEE Trans. Power Electron.*, vol. 27, no. 11, pp. 4734–4749, Nov. 2012.

[4] T. Liu, X. Wang, F. Liu, K. Xin, and Y. Liu, "Islanding detection of grid-forming inverters: Mechanism, methods, and challenges," *IEEE Electrific. Mag.*, vol. 10, no. 1, pp. 30–38, Mar. 2022.
[5] M. Ganjian-Aboukheili, M. Shahabi, Q. Shafiee, and J. M. Guerrero, "Seamless transition of microgrids operation from grid-connected to islanded mode," *IEEE Trans. Smart Grid*, vol. 11, no. 3, pp. 2106–2114, May 2020.
[6] O. V. Kulkarni, S. Doolla, and B. G. Fernandes, "Mode transition control strategy for multiple inverter-based distributed generators operating in grid-connected and standalone mode," *IEEE Trans. Ind. Appl.*, vol. 53, no. 6, pp. 5927–5939, Nov./Dec. 2017.
[7] Z. Liu, J. Liu, and Y. Zhao, "A unified control strategy for three-phase inverter in distributed generation," *IEEE Trans. Power Electron.*, vol. 29, no. 3, pp. 1176–1191, Mar. 2014.
[8] X. Meng, X. Liu, M. He, Z. Liu, and J. Liu, "A self-adaptive controller for inverter with seamless transfer and automatic pre-synchronization capability," *IEEE Access*, vol. 8, pp. 105936–105949, 2020.
[9] T. Liu and X. Wang, "Physical insight into hybrid-synchronization-controlled grid-forming inverters under large disturbances," *IEEE Trans. Power Electron.*, vol. 37, no. 10, pp. 11475–11480, Oct. 2022.
[10] X. Meng, Z. Liu, H. Zheng, and J. Liu, "A universal controller under different operating states for parallel inverters with seamless transfer capability," *IEEE Trans. Power Electron.*, vol. 35, no. 9, pp. 9794–9812, Sep. 2020.
[11] Z. Liu and J. Liu, "Indirect current control based seamless transfer of three-phase inverter in distributed generation," *IEEE Trans. Power Electron.*, vol. 29, no. 7, pp. 3368–3383, Jul. 2014.
[12] H. Kim, T. Yu, and S. Choi, "Indirect current control algorithm for utility interactive inverters in distributed generation systems," *IEEE Trans. Power Electron.*, vol. 23, no. 3, pp. 1342–1347, May 2008.
[13] X. Meng, H. Guo, X. Wang, M. He, and J. Liu, "Seamless transition for parallel inverters with novel self-adaptive hybrid controller and pre-synchronization unit," *IEEE J. Emerg. Sel. Topics Power Electron.*, vol. 10, no. 5, pp. 5819–5832, Oct. 2022.
[14] J. Merino, P. Mendoza-Araya, G. Venkataramanan, and M. Baysal, "Islanding detection in microgrids using harmonic signatures," *IEEE Trans. Power Del.*, vol. 30, no. 5, pp. 2102–2109, Oct. 2015.
[15] A. S. Aljankawey, W. G. Morsi, L. Chang, and C. P. Diduch, "Passive method-based islanding detection of renewable-based distributed generation: The issues," in *Proc. IEEE Elect. Power Energy Conf.*, 2010, pp. 1–8.
[16] Z. Ye, A. Kolwalkar, Y. Zhang, P. Du, and R. Walling, "Evaluation of anti-islanding schemes based on nondetection zone concept," *IEEE Trans. Power Electron.*, vol. 19, no. 5, pp. 1171–1176, Sep. 2004.
[17] N. Liu, A. Aljankawey, C. Diduch, L. Chang, and J. Su, "Passive islanding detection approach based on tracking the frequency-dependent impedance change," *IEEE Trans. Power Del.*, vol. 30, no. 6, pp. 2570–2580, Dec. 2015.
[18] M. E. Ropp, M. Begovic, and A. Rohatgi, "Analysis and performance assessment of the active frequency drift method of islanding prevention," *IEEE Trans. Energy Convers.*, vol. 14, no. 3, pp. 810–816, Sep. 1999.
[19] Q. Sun, J. M. Guerrero, T. Jing, J. C. Vasquez, and R. Yang, "An islanding detection method by using frequency positive feedback based on FLL for single-phase microgrid," *IEEE Trans. Smart Grid*, vol. 8, no. 4, pp. 1821–1830, Jul. 2017.
[20] X. Chen, Y. Li, and P. Crossley, "A novel hybrid islanding detection method for grid-connected microgrids with multiple inverter-based distributed generators based on adaptive reactive power disturbance and passive criteria," *IEEE Trans. Power Electron.*, vol. 34, no. 9, pp. 9342–9356, Sep. 2019.
[21] Y. Zhu et al., "A novel RPV (reactive-power-variation) antiislanding method based on adapted reactive power perturbation," *IEEE Trans. Power Electron.*, vol. 28, no. 11, pp. 4998–5012, Nov. 2013.
[22] S. Murugesan and V. Murali, "Disturbance injection based decentralized identification of accidental islanding," *IEEE Trans. Ind. Electron.*, vol. 67, no. 5, pp. 3767–3775, May 2020.
[23] M. Liu et al., "Compatibility issues with irregular current injection islanding detection methods in multi-DG units equipped with grid-connected transformers," *IEEE Trans. Power Electron.*, vol. 37, no. 3, pp. 3599–3616, Mar. 2022.
[24] D. Voglitsis, F. Valsamas, N. Rigogiannis, and N. Papanikolaou, "On the injection of sub/inter-harmonic current components for active anti-islanding purposes," *Energies*, vol. 11, no. 9, 2018, Art. no. 2183.
[25] K. Jia, H. Wei, T. Bi, D. W. P. Thomas, and M. Sumner, "An islanding detection method for multi-DG systems based on high-frequency impedance estimation," *IEEE Trans. Sustain. Energy*, vol. 8, no. 1, pp. 74–83, Jan. 2017.
[26] D. Reigosa, F. Briz, C. Blanco, P. García, and J. Manuel Guerrero, "Active islanding detection for multiple parallel-connected inverter-based distributed generators using high-frequency signal injection," *IEEE Trans. Power Electron.*, vol. 29, no. 3, pp. 1192–1199, Mar. 2014.
[27] D. Reigosa, F. Briz, C. B. Charro, P. Garcia, and J. M. Guerrero, "Active islanding detection using high-frequency signal injection," *IEEE Trans. Ind. Appl.*, vol. 48, no. 5, pp. 1588–1597, Sep./Oct. 2012.
[28] A. V. Timbus, R. Teodorescu, F. Blaabjerg, and U. Borup, "Online grid impedance measurement suitable for multiple PV inverters running in parallel," in *Proc. 21st Annu. IEEE Appl. Power Electron. Conf. Expo.*, 2006, pp. 907–911.
[29] M. Liu, W. Zhao, S. Huang, K. Shi, and Q. Wang, "Synchronization issues with irregular current injection islanding detection methods in multi-DG operation," in *Proc. IEEE 3rd Int. Conf. Green Energy Appl.*, 2019, pp. 21–29.
[30] M. Liu, W. Zhao, Q. Wang, S. Huang, and K. Shi, "Compatibility issues with irregular current injection islanding detection methods and a solution," *Energies*, vol. 12, no. 8, 2019, Art. no. 1467.
[31] F. Briz, D. Díaz-Reigosa, C. Blanco, and J. M. Guerrero, "Coordinated operation of parallel-connected inverters for active islanding detection using high-frequency signal injection," *IEEE Trans. Ind. Appl.*, vol. 50, no. 5, pp. 3476–3484, Sep./Oct. 2014.
[32] F. Nejabatkhah and Y. W. Li, "Overview of power management strategies of hybrid AC/DC microgrid," *IEEE Trans. Power Electron.*, vol. 30, no. 12, pp. 7072–7089, Dec. 2015.
[33] P. Rodríguez, A. Luna, I. Candela, R. Mujal, R. Teodorescu, and F. Blaabjerg, "Multiresonant frequency-locked loop for grid synchronization of power converters under distorted grid conditions," *IEEE Trans. Ind. Electron.*, vol. 58, no. 1, pp. 127–138, Jan. 2011.
[34] B. Liu, T. Wu, Z. Liu, and J. Liu, "A small-AC-signal injection-based decentralized secondary frequency control for droop-controlled islanded microgrids," *IEEE Trans. Power Electron.*, vol. 35, no. 11, pp. 11634–11651, Nov. 2020.
[35] K. De Brabandere, B. Bolsens, J. Van den Keybus, A. Woyte, J. Driesen, and R. Belmans, "A voltage and frequency droop control method for parallel inverters," *IEEE Trans. Power Electron.*, vol. 22, no. 4, pp. 1107–1115, Jul. 2007.
[36] *IEEE Standard for Interconnection and Interoperability of Distributed Energy Resources with Associated Electric Power Systems Interfaces*, IEEE Standard 1547-2018, 2018.
[37] *IEEE Recommended Practice and Requirements for Harmonic Control in Electric Power Systems*, IEEE Standard 519-2014 (Revision of IEEE Std 519-1992), 2014.
[38] L. Wang, H. Gu, H. Ou, and X. Dou, "A voltage stability control based on impedance estimation for the independent microgrid," in *Proc. IEEE Int. Power Electron. Appl. Conf. Expo.*, 2018, pp. 1–5.
[39] B. Liu, Z. Liu, and J. Liu, "A noninvasive feeder impedance estimation method for parallel inverters in microgrid based on load harmonic current," *IEEE Trans. Power Electron.*, vol. 36, no. 7, pp. 7354–7359, Jul. 2021.
[40] K. Moffat, M. Bariya, and A. V. Meier, "Network impedance estimation for microgrid control using noisy synchrophasor measurements," in *Proc. IEEE 19th Workshop Control Model. Power Electron.*, 2018, pp. 1–6.

Haoyang Zheng (Graduate Student Member, IEEE) received the B.S. degree in electrical engineering from Xi'an Jiaotong University, Xi'an, China, in 2017, and the M.S. degree in general engineering from École Centrale de Lille, Villeneuve d'Ascq, France, in 2020. He is currently working toward the Ph.D. degree in electrical engineering with Xi'an Jiaotong University, Xi'an, China.

His research interests include control of inverters in distributed generation systems.

Zeng Liu (Senior Member, IEEE) received the B.S. degree from Hunan University, Changsha, China, in 2006, and the M.S. and Ph.D. degrees from Xi'an Jiaotong University (XJTU), Xi'an, China, in 2009 and 2013, respectively, all in electrical engineering.

He then joined as a Faculty Member in electrical engineering with XJTU, where he is currently an Associate Professor. From 2015 to 2017, he was with the Center for Power Electronics Systems, Virginia Polytechnic Institute and State University, Blacksburg, VA, USA, as a Visiting Scholar. His research interests include control and stability of power electronics systems with multiple converters for renewable energy and energy storage applications.

Dr. Liu was the recipient of two Prize Paper Awards in IEEE TRANSACTIONS ON POWER ELECTRONICS. He is currently an Associate Editor for the IEEE OPEN JOURNAL OF POWER ELECTRONICS and on the Editorial Board for the *Energies*, and served as Secretary-General for 2019 IEEE 10th International Symposium on Power Electronics for Distributed Generation Systems and 2020 The 4th International Conference on HVDC.

Ronghui An (Member, IEEE) received the B.S. degree in electrical engineering and automation in 2016 from Xi'an Jiaotong University, Xi'an, China, where he is currently working toward the Ph.D. degree.

His research interests include coordinative control of distributed generations in microgrid systems, and design and control of grid-interlinking converter.

Jinjun Liu (Fellow, IEEE) received the B.S. and Ph.D. degrees in electrical engineering from Xi'an Jiaotong University (XJTU), Xi'an, China, in 1992 and 1997, respectively.

He then joined the Electrical Engineering School, XJTU, as a Faculty Member. From late 1999 to early 2002, he was with the Center for Power Electronics Systems, Virginia Polytechnic Institute and State University, Blacksburg, VA, USA, as a Visiting Scholar. In late 2002, he was promoted to a Full Professor and then the Head of the Power Electronics and Renewable Energy Center, XJTU, which now comprises more than 20 faculty members and more than 200 graduate students and carries one of the leading power electronics programs in China. From 2005 to early 2010, he served as an Associate Dean of the Electrical Engineering School, XJTU, and from 2009 to early 2015, the Dean for Undergraduate Education of XJTU. He is currently a XJTU Distinguished Professor of Power Electronics. He coauthored 3 books (including 1 textbook), published more than 500 technical papers in peer-reviewed journals and conference proceedings, holds more than 70 invention patents (China/US/EU), and delivered for many times plenary keynote speeches and tutorials at IEEE conferences or China national conferences. His research interests include modeling, control, and design methods for power converters and electronified power systems, power quality control and utility applications of power electronics, and micro-grids for sustainable energy and distributed generation.

Dr. Liu received for many times governmental awards at national level or provincial/ministerial level for scientific research/teaching achievements. He also received the 2006 Delta Scholar Award, the 2014 Chang Jiang Scholar Award, the 2014 Outstanding Sci-Tech Worker of the Nation Award, the 2016 State Council Special Subsidy Award, the IEEE Transactions on Power Electronics 2016 and 2021 Prize Paper Awards, the Nomination Award for the Grand Prize of 2020 Bao Steel Outstanding Teacher Award, and the 2022 Fok Ying Tung Education and Teaching Award. He served as the IEEE Power Electronics Society Region 10 Liaison and then China Liaison for 10 years, an Associate Editor for the IEEE TRANSACTIONS ON POWER ELECTRONICS since 2006, 2015–2019 Executive Vice President and 2020–2021 Vice President of IEEE PELS. He was on the Board of China Electrotechnical Society 2012–2020 and was elected the Vice President in 2013 and the Secretary General in 2018 of the CES Power Electronics Society. He was 2013–2021 Vice President for International Affairs, China Power Supply Society (CPSS), and since 2016, the inaugural Editor-in-Chief of CPSS Transactions on Power Electronics and Applications. He was elected the President of CPSS in November 2021. Since 2013, he has been serving as the Vice Chair of the Chinese National Steering Committee for College Electric Power Engineering Programs.

Tong Wu (Student Member, IEEE) received the B.S. degree in electrical engineering, in 2019, from Xi'an Jiaotong University, Xi'an, China, where he is currently working toward the Ph.D. degree.

His research interests include modeling and control of voltage source converters and small-signal stability analysis of ac power electronics systems.

Zhenhuang Lin was born in 1984. He received the master's degree in electrical engineering from Fuzhou University, Fuzhou, China, in 2019.

His research interests focus on high power bidirectional converters for energy storage systems and solar inverters.